Asian Journal of Pharmaceutical Sciences 17 (2022) 284–297

Available online at www.sciencedirect.com

ScienceDirect

journal homepage: www.elsevier.com/locate/AJPS

Original Research Paper

Design and fabrication of r-hirudin loaded dissolving microneedle patch for minimally invasive and long-term treatment of thromboembolic disease

Mengfang Wu[a,b], *Tian Xia*[a,b], *Yaran Li*[a,b], *Tianfa Wang*[a,b], *Shijia Yang*[a,b], *Jinchao Yu*[a,b], *Qiaoyan Liang*[a,b], *Teng Shen*[c,*], *Min Yu*[a,b,*], *Bing Zhao*[a,b,*]

[a] *Key Laboratory of Metabolism and Molecular Medicine, Ministry of Education, Fudan University, Shanghai 200032, China*
[b] *The Department of Biochemistry and Molecular Biology, School of Basic Medical Sciences, Fudan University, Shanghai 200032, China*
[c] *Key Laboratory of Smart Drug Delivery, Ministry of Education, Department of Pharmaceutics, School of Pharmacy, Fudan University, Shanghai 201203, China*

ARTICLE INFO

Article history:
Received 28 October 2021
Revised 12 January 2022
Accepted 26 February 2022
Available online 21 March 2022

Keywords:
Anticoagulant
r-hirudin
Microneedle patch
3D printing technology

ABSTRACT

Cardiovascular disease is the leading cause of global mortality, with anticoagulant therapy being the main prevention and treatment strategy. Recombinant hirudin (r-hirudin) is a direct thrombin inhibitor that can potentially prevent thrombosis via subcutaneous (SC) and intravenous (IV) administration, but there is a risk of haemorrhage via SC and IV. Thus, microneedle (MN) provides painless and sanitary alternatives to syringes and oral administration. However, the current technological process for the micro mould is complicated and expensive. The micro mould obtained via three-dimensional (3D) printing is expected to save time and cost, as well as provide a diverse range of MNs. Therefore, we explored a method for MNs array model production based on 3D printing and translate it to micro mould that can be used for fabrication of dissolving MNs patch. The results show that r-hirudin-loaded and hyaluronic acid (HA)-based MNs can achieve transdermal drug delivery and exhibit significant potential in the prevention of thromboembolic disease without bleeding in animal models. These results indicate that based on 3D printing technology, MNs combined with r-hirudin are expected to achieve diverse customizable MNs and thus realize personalized transdermal anticoagulant delivery for minimally invasive and long-term treatment of thrombotic disease.

* Corresponding authors.
E-mail addresses: shenteng@fudan.edu.cn (T. Shen), minyu@shmu.edu.cn (M. Yu), zhaobing@fudan.edu.cn (B. Zhao).
Peer review under responsibility of Shenyang Pharmaceutical University.

https://doi.org/10.1016/j.ajps.2022.02.005

1. Introduction

Anticoagulant therapy is one of the most common forms of medical intervention used for the treatment and prevention of arterial and venous thromboembolism [1]. Routes for traditional anticoagulant administration mainly include parenteral (IV and SC) and oral administration. However, oral administration of anticoagulants may cause gastrointestinal bleeding, especially for those who had basic gastrointestinal diseases, and decrease utilization rates after gastrointestinal degradation and liver metabolism [2,3]. In addition, pain, ecchymosis and hematoma are common side effects of injection [4]. Most importantly, this method produces a considerable amount of medical waste that is both environmentally unfriendly and carries a risk of secondary infection [5], greatly limiting the clinical applicability of anticoagulants.

Thrombin, a serine protease, plays a central role in both physiological haemostatic and pathological thrombotic processes, thus providing a core target for anticoagulant therapy. R-hirudin is a direct thrombin inhibitor produced by our laboratory. A previous study revealed that r-hirudin has a high affinity and specificity for thrombin [6]. However, in clinical trials, r-hirudin was administered via IV or SC injection [7], which is usually accompanied by postoperative bleeding, poor patient compliance, and inconvenience of daily medication, thus severely restricting its clinical application. Microneedles (MNs) are promising alternatives based on their potential advantages [4].

MNs patch (MNP) refers to an MNs array with needle lengths less than 1000 μm that can penetrate the cuticle and release the drug without damaging the blood vessels and nerves in the dermis [8]. Potential advantages include continuous controlled drug release, reduced side effects, lower drug dose required, and less invasive dosing [9]. Previous reports state that biodegradable polymer-based dissolvable MNs (DMN) can load drugs without loss of activity and provide controlled-release delivery in the skin for hours to months [10,11]. MN-mediated transdermal drug delivery is extensively used in various chemicals and biologicals [12–17]. Although most are vaccines, such as those for rabies [18], measles [19], and canine influenza [20], and small molecule compounds, such as vitamin K [21], there are still some protein drugs that have achieved transdermal drug delivery, including insulin [22], human growth hormone [23], small molecule heparin [24] and antibodies like IgG [25]. These results indicate that r-hirudin, a protein drug, can be loaded in biodegradable polymer and achieve transdermal delivery via MNs. This administration route would significantly improve patient compliance and largely prevent the side effects caused by IV and SC injections. Although many benefits are provided by MNs, challenges must be overcome to achieve a clinically acceptable drug delivery device. The dosage of dissolving microneedles (DMN) is affected by the physical stability and mechanical strength of the microneedles themselves, which may lead to inaccurate administration or poor repeatability, and some drugs with strict requirements on the accuracy of administration may be excluded [26,27]. Furthermore, MNs often suffer from insufficient skin insertion, the insertion of MNs into the skin was affected by many factors such as geometry, materials of MNs, and skin conditions of study objects, which would also lead to poor repeatability [28]. Further study showed that the reasonable combination of different materials can realize the layering of the microneedles so that the loaded drugs are concentrated in the tip, which greatly saves drugs and prevents waste [29,30].

Notably, the existing models used for MN mould fabrication are mainly based on the photo etching of silicon materials, although novel methods for model fabrication have also emerged [31]. Most of these production processes for fabricating MNs array master templates are relatively complex and complicated, which to some extent limits the advances of MNs for medical applications. High-precision three-dimensional (3D) printing is a novel method of solid micromodel construction via stereo stacking on a two-dimensional plane. However, this method is still in its nascent stages in the pharmaceutical industry. In 2016, the first 3D printed pharmaceutical product was approved by the United States Food and Drug Administration [32]. Currently, with the improvement of printing accuracy, high-precision micro 3D printing introduces a new era [33–38]. This enables the target micro mold to be easily obtained within hours through computer simulation and output for printing, largely simplifying the process of micro mold fabrication and saving time and cost.

Here, we introduced a method for MNs array model production via 3D printing technique and translated the 3D printed MNs array model into a female PDMS mould, which can be directly used for microneedle fabrication via micro-molding. Combined r-hirudin, a direct thrombin inhibitor produced by our laboratory and usually administrated via IV injection, with 3D printing originated MNs is expected to facilitate minimally invasive and painless administration of anticoagulants, ultimately resulting in improved patient compliance and reduced side effects. Further, with high economic and social advantages, it is expected to realize the industrialization of the anticoagulant microneedle.

2. Materials and methods

2.1. *Materials*

Thrombin, polyvinylpyrrolidone K-90 (PVP K-90; MW = 360 kDa) and carboxymethyl cellulose (CMC) were obtained from Sigma-Aldrich (St. Louis, MO). R-hirudin was produced in our laboratory. Low molecular weight hyaluronic Acid (LMHA, ~ 44 kDa) was purchased from Bloomage Freda Biopharm (Jinan, China), and Gantrez™S-97 (GAS) was purchased from Ashland (Tadworth, Surrey, UK). Methylene blue (MB) was purchased from Sigma-Aldrich (Steinheim, Germany). Polydimethylsiloxane (PDMS, Sylgard 184) was purchased from Dow Corning, (Midland, MI) [39]. Collagen type I (3.77 mg/ml) was purchased from Discovery Labware (MA 01730, USA). Rhodamine 6 G was purchased from Aladdin. All other chemicals were of analytical grade, and all solvents used were of high-performance liquid chromatography (HPLC) grade.

2.2. Animals

All Sprague-Dawley (SD) rats and C57/BL6 mice were purchased from the Animal Center of Fudan University. All animal studies were conducted following the rules and regulations of the IACUC at the Department of Laboratory Animal Science, Fudan University (Shanghai, P.R. China). Fresh porcine ears were purchased from slaughterhouse (Shanghai, P.R. China).

2.3. Model design and print

The MNs array model was designed with an overall dimension of 10×10 MNs per array. Considering the limitation of 3D printing accuracy that would result in the tip loss of MNs, the MNs were designed to be 1000 μm high, with 200 μm that could be discounted due to tip loss and arrayed in the vertical direction of a 10 mm × 10 mm patch. To improve the piercing ability, MNs were designed into a pyramid shape, and the side lengths of the two different MNs labeled MN1# and MN2# were 150 μm and 100 μm, respectively. A computer drawing of the MNs array model was created using Rhino 6.0, in stereolithography file format. A high-precision printing system, the NanoArch P140 system, was selected for 3D printing with an accuracy of approximately 10 μm. The finished STL file was transferred to a NanoArch P140 printer and the MNs array was printed in the photosensitive resin because it can be cured and modeled under ultraviolet light at a UV-LED wavelength of 405 nm. The printed MNs lengths were then measured using a stereomicroscope (Olympus Mvx10, Japan).

2.4. Reproduction of 3D printing model

The 3D printing model was replicated using PDMS by selecting gelatine as an intermediate transition material. Gelatine was melted at 55–60 °C at a concentration of 12% (w/v). The printed MNs array model was fixed at the bottom of a small culture dish and cast with 12% (w/v) gelatine to completely cover it, and the bubbles produced during the casting process were defoamed in a thermostatic water bath using a vacuum drying chamber (DZF-6012, Shanghai, China) before the gelatine solidified. After solidification at 25 °C, the printing model was demoulded from the gelatine, and a pinhole array in the solidified gelatine model was obtained. Then, PDMS was cast into the pinhole array of the gelatine model and fully defoamed in a vacuum drying chamber. After curing at 25 °C for 2–3 d, the MNs array on PDMS was obtained. After silanization treatment for 15–30 min, PDMS was cast onto the PDMS model again and solidified at 60 °C for ≥ 2 h to obtain a female PDMS mould that can be used for direct MNP fabrication.

2.5. Preparation of reagents

HA was selected as the r-hirudin loading material because it can be easily obtained and widely distributed in organisms; thus, it exhibits good biocompatibility and biodegradability [40]. Different concentrations of HA, r-hirudin, and GAS were tested, GAS was used as a crosslinking agent to build a network between HA molecules. The optimized HA and GAS concertations were determined to be 10% (w/v) and 1% (w/v), respectively, and the optimum concentration range of r-hirudin was 1–20 mg/ml. HA-GAS-r-hirudin solution was thoroughly mixed with an ultrasonic cleaner (SK7210HP, Shanghai, China), and the remaining bubbles were further removed via a vacuum drying chamber.

2.6. Fabrication of the microneedle

The PDMS mould was cleared with absolute ethanol and dried in the bellows. The mixed solution previously prepared above was cast into the model, and the MN holes in the PDMS model were filled via vacuum extraction and this process was repeated until all of the holes were filled. The casting solution was then dried at 25 °C for one or two days, and r-hirudin-loaded MNPs were finally obtained by demoulding from the PDMS mould.

2.7. Characterisation of microneedle

To characterize the properties of the 3D printing-based MNs, strength tests were performed using a dynamometer (TA.XT Plus, UK). The downward distance was set to 600 μm with a uniform downward velocity of 1 mm/s. A total of 15 MNs were tested under one probe each time, and the triggering force was set at 0.049 N. Distance-strength curves were drawn to determine the intensity of a single MN. Inverted fluorescence microscopy (Olympus Mvx10, Japan) were used for the morphological detection of MNs. Rhodamine 6 G or methylene blue was added separately to the fabrication process for better observation.

2.8. Drug loading capacity of microneedle

The MNs with various amounts of r-hirudin loaded were separated from the MNP using a knife blade and dissolved in 1 ml phosphate-buffered saline (PBS, pH 7.4), diluted to an appropriate concentration, and then the drug-loading capacity can be calculated according to the anticoagulant activity of the dissolved solution and BCA protein quantitative analysis was also conducted to further quantifying the loading capacity of 3DMN, each group was repeated three times.

2.9. Release profiles of the r-hirudin loaded microneedle patch

R-hirudin with different concentration (1 mg/ml, 2.5 mg/ml, 5 mg/ml) was fully mixed with 10% (w/v) HA and 1% GAS, and various amount of HA (10%, 15% and 20%, w/v) with or without 1% GAS was fully mixed with 2.5 mg/ml r-hirudin soultion. The mixture of r-hirudin, HA, and GAS were then used for MN fabrication after defoaming via ultrasound and vacuum. MNs was demoulded after drying at 25 °C that assisted by a dehumidifier. Each MN patch was, respectively placed into a 5 ml tube that containing 3 ml PBS and gently waggled on a shaking bed (10 rpm, 25 °C). A total of 50 μl sample was collected at different time points (0, 15, 30, 60, 120, 180, 300, 420 min) and supplemented with 50 μl PBS after sampling immediately each time. BCA protein quantification

was conducted to quantitative analysis of r-hirudin released in the PBS. MNs and patch were also separated to further compare the release profile of patch and MNs. Each group was repeated three times.

2.10. Preparation of skin

Hair on the rat skin was carefully shaved by an electric clipper, the remaining hairs were further cleared using depilatory cream, then the subcutaneous fat and muscle tissue were gently removed using ophthalmic scissors. The hair on the porcine cadaver skin and the fat and muscle tissue under the skin was gently removed by ophthalmic scissors. Finally, the intact skin after trimming was prepared for further transdermal delivery of r-hirudin loaded MNs *in vitro*.

2.11. Penetration efficiency of microneedle

The MN penetration efficiency was investigated using an *in vitro* model previously reported [41]. Parafilm M was folded into eight layers (thickness: ~1 mm) without stretching, then placed on a hard flat plate. The MN patch was placed on the folded parafilm and pressed with a homemade drug dispenser for 30 s. Then, the parafilm was unfolded and the number of penetrated holes in each layer was counted. Further studies were also performed on porcine cadaver skin or SD rat skin, and the micro holes created by MNs loaded with rhodamine 6 G were then counted by the naked eye. In addition, the penetration depth was also detected via Confocal Laser Scanning Microscopy (CLSM, Carl Zeiss LSM710, Germany), the image was recorded at the scanning surface every 10 μm, and the scan was beginning or stopped when no fluorescence signal was detected. A freezing microtome section was conducted to observe the penetration depth more intuitively.

2.12. Transdermal drug delivery in vitro

The SC tissue and fat of porcine cadaver skin or rat skin were carefully removed to prepare for subsequent experiments. A TK-20A diffusion instrument was used to simulate the microenvironment of an organism, and a small receiving pool below was used to simulate the SC local environment dominated by blood vessels. Every single r-hirudin-loaded MN patch (75 μg) or the same amount of r-hirudin solution was, respectively administrated to each piece of pig or rat skin ($n = 4$). The patches were then removed after 5 min administration, remaining microneedle body on the patch was collected to quantify the remaining r-hirudin that were not administrated, therefore, the dosing rate (the amount of r-hirudin administrated into skin via microneedles/total amount) can be calculated according to the remaining drug on the residual microneedle body. The small chamber under the skin was filled with PBS (2 ml), and a stir bar was placed to generate the fluid force, the stirring speed was set to 167 rpm, the water bath temperature was set to 37 °C. The amount of r-hirudin released in the lower chamber was, respectively measured at 0, 0.5, 1, 1.5, 2, 3, 5,7 and 9 h via thrombin titration, and the chamber was supplemented with 50 μl PBS immediately at the end of sampling (50 μl). Finally, a time-release curve was drawn to observe the drug release dynamics.

2.13. Skin resealing assay

The abdominal hair of Sprague-Dawley rats was removed before dosing, and each rat was administrated one MN patch by pressing it onto the skin for 15 s, then peeling off the patch after 5 min administration. Photographs were taken to record skin conditions such as erythema, wounds, and spots before and after administration. Skin recovery was observed four days later by observing the presence of hair regrowth or an invasive wound [42].

2.14. Subcutaneous hemorrhage test post administration

C57BL/6 mice (20±0.5 g, male) were selected for subcutaneous hemorrhage analysis. Mice were anesthetized with 10% chloral hydrate, hair on the back neck was cleared up using depilatory cream. Depilatory cream was then gently scrubbed after 2 min treatment using cotton balls soaked in 37 °C normal saline. Mice were divided into 4 groups (control, blank-MN, r-hirudin-SC, r-hirudin-MN) of which the control group was not treated, the other three groups were, respectively treated with blank-MN, r-hirudin-SC and r-hirudin-MN. Each mouse were treated three times with an administrating interval of 0.5 h. Finally, mice were killed by neck amputation, skin with treatment was isolated and fixed in 4% formaldehyde. Subcutaneous hemorrhage was analyzed by observation and recorded by a photograph.

2.15. Transdermal drug delivery in vivo

Sprague-Dawley rats (200±20 g, male) were selected for further study, r-hirudin SC injection and MN administration were compared to saline treatment in SD rats. In groups 1, 2, and 3, rats were treated with saline ($n = 6$), r-hirudin via SC injection (0.5 mg/kg, $n = 8$), and r-hirudin via MN administration (30 μg/patch, 4 patch/rat, $n = 7$), respectively. The patches were then removed after 5 min administration, remaining microneedle body on the patch was collected to quantify the remaining r-hirudin that were not administrated, therefore, the dosing rate can be calculated according to the remaining drug on the patch. Blood samples were collected before treatment and 0.5, 1, 1.5, 2, 3, 4, 5, 6, and 7 h after treatment from the carotid artery and pre-treated with 3.8% sodium citrate at a ratio of 1:9 (v/v). Plasma was obtained by centrifuging at 4500 rpm for 10–15 min and transferred to a fresh tube; aPTT, PT, and TT were measured using a full-automatic blood coagulation apparatus (Sysmex CA-1500, Japan). Liquid chromatography-mass spectrometry (LC-MS, Agilent G1946D Quadrupole Plain Detector) was also conducted to directly detect the change in concentration of r-hirudin in rats serum for bioavailability analysis based on previously established methods [43].

2.16. Establishment of acute pulmonary embolism model

C57BL/6 mice (18±0.5 g, male) were administered saline ($n = 10$), r-hirudin SC injection ($n = 13$), and r-hirudin loaded

MN administration ($n = 13$). Thirty minutes later, the mice were injected with a 175 µl mixture of recombinant collagen (3.6 mg/ml) and epinephrine (0.03 mg/ml) via the tail vein and were scanned via CT (Inveon PET/PT) before and after injection. The death rate was recorded within 5 min. Histological studies were performed on the lungs fixed in 4% formaldehyde, and paraffin sections were stained with hematoxylin/eosin.

2.17. Establishment of mesenteric artery thrombosis model

Intravital microscopy was performed according to a previously reported method [44] with minor modifications. Blood (0.9 ml) was harvested from the abdominal aorta of chloral hydrate-anaesthetized C57BL/6 mice (8 weeks old, male) into syringes containing 0.1 ml of 3.8% sodium citrate. Blood was collected in a 15 ml fresh tube and diluted with half-blood-volume 0.9% NaCl. Platelet-rich supernatant was obtained by centrifugation at 300 g for 3 min and transferred to a 15 ml fresh tube, an additional half-blood-volume 0.9% NaCl was added to the blood. The remaining platelet-rich supernatant was harvested after centrifugation at 300 g for 3 min. Platelets were obtained by centrifugation of platelet-rich supernatant at 510 g for 3 min. Pellets were resuspended in HEPES-Tyrode buffer and incubated with 8 µg/ml calcein-AM at 37 °C for 30 min to label the platelets. After centrifugation at 510 g for 3 min, the marked platelets were collected and resuspended in HEPES-Tyrode buffer at 37 °C. Mice (C57BL/6 mice, 8 weeks old) were treated with saline and r-hirudin via SC injection or MN administration. Calcein-labeled platelets ($4–5 \times 10^9$ /kg) were delivered into the treated mice via the tail vein. After 30 min, recipient mice were anesthetized with chloral hydrate, and the mesentery was exteriorized gently through a midline abdominal incision. The injury was induced by topical application of a 1×4 mm filter paper saturated with 10% ferric chloride for 1 min and recorded using intravital microscopy. We recorded the ratio of emboli formation and the length of fluorescence that formed by the platelets labeled at 10 min.

2.18. Fabrication of double-layer microneedle patch

To save drugs to the maximum and avoid drug waste in the patch, we further developed a double-layer microneedle patch and choose PVP as the material for patch fabrication. PVP was dissolved in absolute alcohol and heated in a 70 °C-water bath to accelerate dissolution for preparation of the back material with a final concentration of 20% (w/v). HA-GAS-r-hirudin solution was prepared and cast in a model followed by vacuum extraction to fill the MN holes. This process was repeated until all of the holes were filled as mentioned above. The residual solution was then recycled and HA-GAS- r-hirudin solution was cast again after drying at 25 °C for 2 h. Vacuum extraction was performed to further fill the MN holes, the residual solution was recycled again, and 20% PVP was then cast to serve as the back of the MN patch. The casting model was dried at 25 °C for 1–2 d to obtain the final double-layer drug-loaded MNPs.

2.19. Statistical analysis

All data were expressed as the mean ± SD. Differences between the groups were analyzed by two-way and one-way analysis of variance, followed by a Tukey's test for multiple comparisons. Fisher's exact test was used to compare survival rates. Statistical analysis was performed using Prism software (version 7.0; GraphPad Inc., San Diego, CA, USA). Statistical significance was set at $p < 0.05$.

3. Results and discussion

3.1. Design and print of microneedles array

The designed MN1# and MN2# array model and its stereolithography format file were shown in Fig. 1A and 1B. They were designed to be 1000 µm long and arrayed in 10 mm × 10 mm patch. MNs were designed into a pyramid shape, and the side lengths of MN1# and MN2# were 150 µm and 100 µm, respectively that were shown in Fig. 1C and D. A high-precision printing system, the NanoArch P140 system, was selected for 3D printing with an accuracy of approximately 10 µm (Fig. 1D). The printed lengths of MN1# and MN2# were 854 µm and 795 µm, respectively, as measured by optical microscopy (Fig. 1A–1C). These data revealed that MN arrays could be obtained via a high-precision printing system.

3.2. Model reproduction and microneedle fabrication

PDMS has been extensively used in model engraving because of its stable properties and good elasticity [39]. Our previous study demonstrated that PDMS cannot be cured at the contact surface of the photosensitive resin. Thus, agarose, HA, CMC, PVP, and gelatine were compared to screen an appropriate intermediate transition material that could replace the direct use of PDMS, and gelatine was selected as the candidate. The fabricating process was shown in Fig. 2A. R-hirudin-loaded and hyaluronic acid-based MNPs were also fabricated (Fig. 2B). These results indicated that the 3D printed MNs array model can be duplicated via a three-step casting process that is mediated by gelatine.

3.3. Characterization of casting model and HA-based microneedle

To investigate the shape loss from the PDMS model to the final MNs, electron microscope scanning (EMS, FEINova NanoSEM 450, USA) was conducted, and the scanning plane was tilted by 25° for better measurement. The length × width of HA-MN1# and HA-MN2# were 967.8 µm × 145.2 µm and 887.3 µm × 104 µm, respectively (Fig. S1A). A slight shape loss was observed compared to the lithography-model-based MNs (Fig. 1D & S1B). In fact, there was no obvious tip losses. These results indicated that the 3D printed MNs array model could be effectively duplicated by a three-step casting process.

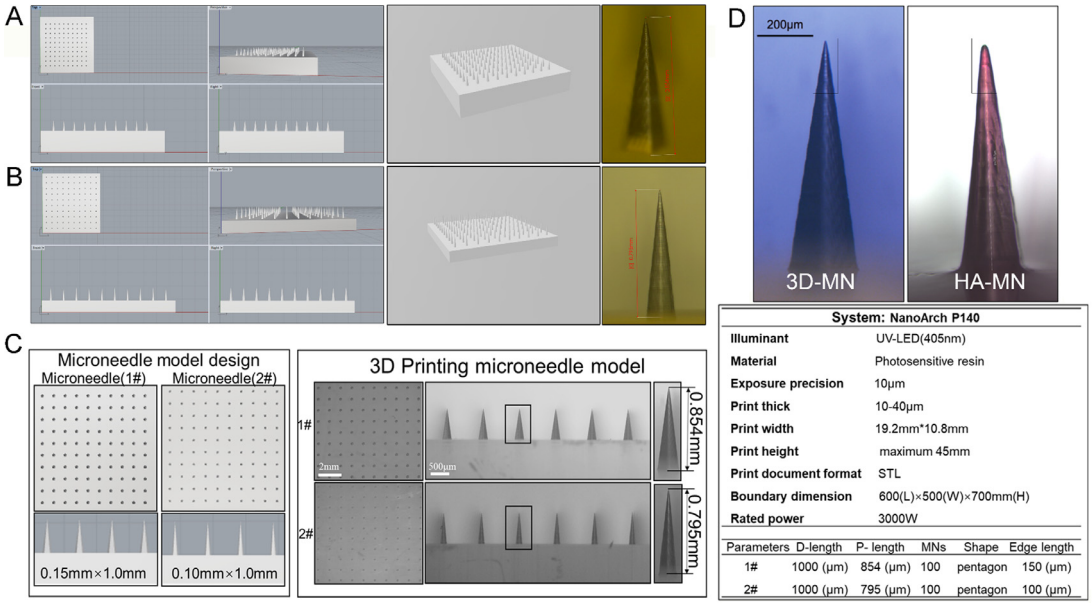

Fig. 1 – Schematic representation of the MNs array model simulation and 3D printing technique. (A) Computer simulation diagram of the MN1# array (left); print preview of the MN1# array (middle); lengths of the printed MN1# (right, red scale bar: 0.854 mm). (B) Computer simulation diagram of the MN2# array (left); print preview of the MN2# array (middle); length of the printed MN2# (right, red scale bar: 0.795 mm). (C) Schematic representation of the designed model and the 3D-printed model. (D) Representative image of 3D print MNs and HA-based MNs that fabricated using PDMS mould via micro-molding (left), specification of the 3D-printing system used for MNs array printing (above) and preset parameter of the MNs array (right).(For interpretation of the references to color in this figure legend, the reader is referred to the web version of this article).

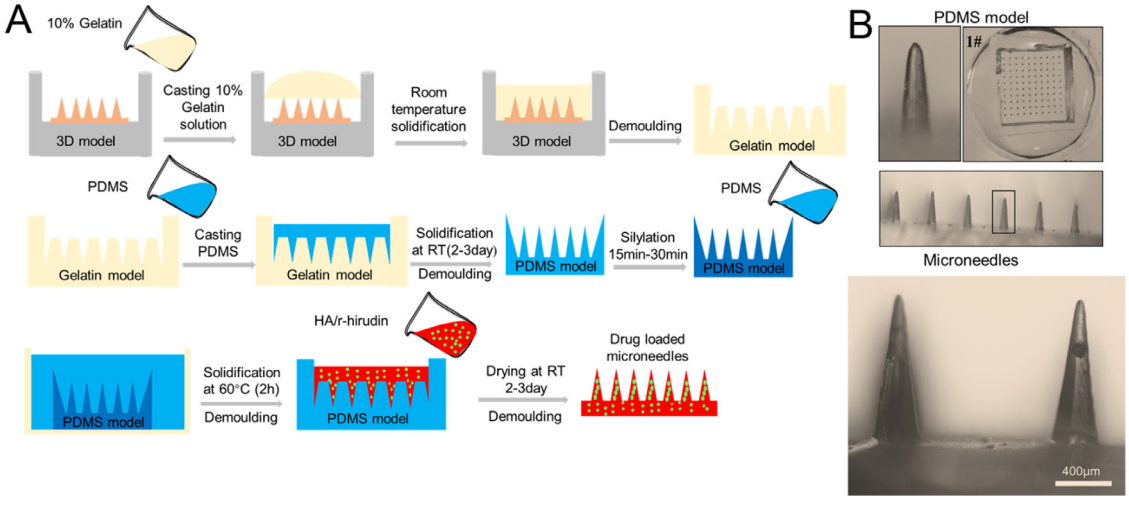

Fig. 2 – Model reproduction and MNs fabrication. (A) Process of model reproduction and MNs fabrication. (B) Schematic representation of PDMS model and MNs that fabricated using PDMS mould.

3.4. *Microneedle properties*

The penetrating ability of MN1# and MN2# on rat skin was compared, and MN1# was selected for further study because it had a much higher skin penetrating ability than MN2# (Fig. 3A, 3D, S2A). MN1# can also penetrate porcine cadaver skin with high efficiency, which further demonstrated its practicability (Fig. 3E). The strength test showed that the average intensity of 3DMNs was obviously higher than 0.058 N per MN [45], which is reportedly sufficient to penetrate the stratum corneum (Fig. 3B). An *in vitro* study of the penetrating depth on parafilm M revealed a minimum penetration depth of ~300 μm (Fig. 3C), and the penetration rate on a rat or porcine cadaver skin was higher than 90% (Fig. 3F). The freezing microtome section and CLSM further confirmed that the penetration depth was around 300 μm (Fig. 4C, S2B). Drug release was

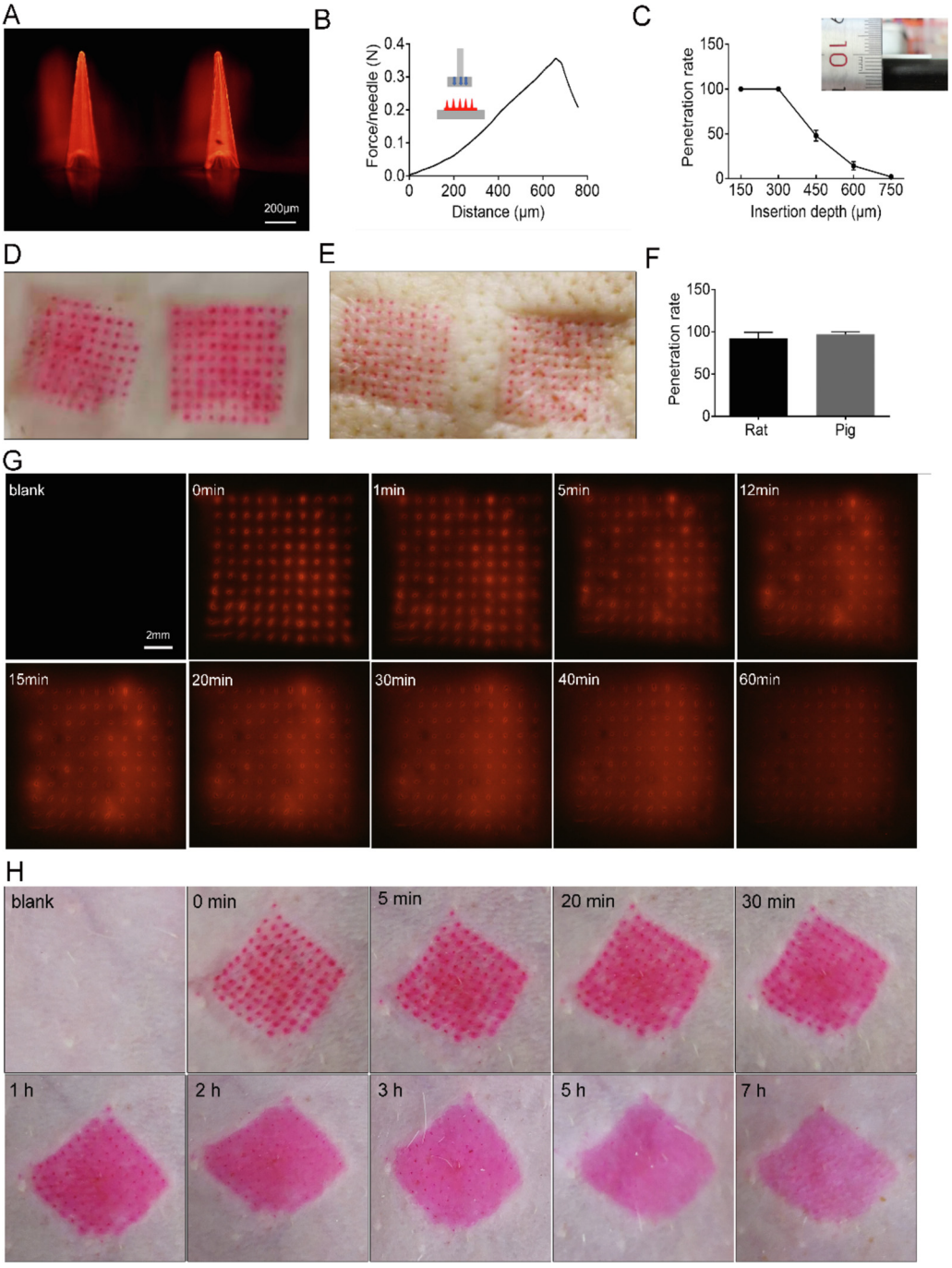

Fig. 3 – Penetrating properties of r-hirudin loaded 3DMN *in vitro*. (A) Representative image of MN1#. (B) Strength test for MN1#. (C) The penetration depth of MN1# on parafilm M. (D) Rat skin puncture image of MN1#. (E) Porcine cadaver skin puncture image of MN1#. (F) Penetration rate of MN1# on rat/porcine skin. (G) Representative images of rhodamine 6 G loaded in MNs release on 1% agarose gel. (H) Wound healing assay of micro-hole created by MNs application *in vivo* on rat skin.

recorded using an *in vitro* model based on 1% agarose gel [46]. The results showed that the dye loaded in the MNs could start releasing within 5 min (Fig. 3G). Similar results were also observed in a skin resealing assay [42], in which rhodamine 6 G loaded MNs could start to diffuse within 5 min post-MN administration, and micro-holes created by MNs on the rat skin could quickly reseal within 5 h (Fig. 3H). All of the data indicated that the MNs array originating from 3D printing could effectively penetrate the body skin and rapidly achieve r-hirudin release without leaving obvious wounds.

The release profiles of 3DMN with different formulations showed that the combination of GAS, and HA at a relatively high ratio in the formula could slow the release of r-hirudin from MNs to PBS (Fig. S3A & S3B). It may be due to GAS, a crosslink agent, mediated the cross-linking of HA molecules, which would provide enhanced stability

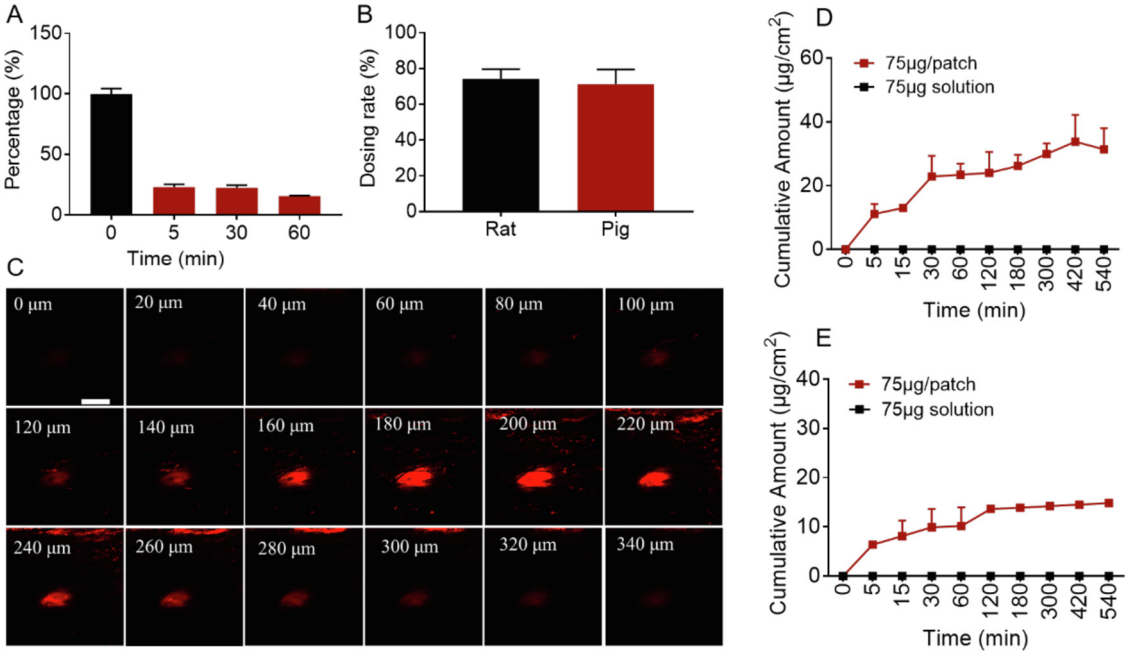

Fig. 4 – Transdermal delivery of r-hirudin via 3DMN administration *in vitro*. (A) The dissolution rate of r-hirudin loaded 3DMN in rat skin with different dissolving times (reflect by the length ratio of MNs residue on patch, $n = 3$). (B) Dosing rate of r-hirudin loaded 3DMN on rat ($n = 4$) and porcine cadaver skin ($n = 4$). (C) Representative images of penetration depth via confocal laser scanning microscopy (bar: 200 μm). (D) Transdermal delivery of r-hirudin loaded 3DMN on rat skin ($n = 4$). (E) Transdermal delivery of r-hirudin loaded 3DMN on porcine cadaver skin ($n = 4$).

to HA-based materials [47]. The drug loading capacity of MNs is shown in Fig. S2C, it is indicated that 3DMN can load a wide range amount of r-hirudin via increasing the content of r-hirudin in the formulations, and the change of r-hirudin content in formulations had no obvious impact on the release profiles of 3DMN (Fig. S3C). Microneedles and patch were separated and the release profiles were also analyzed, respectively, it is showed that there was no obvious difference in release tendency (Fig. S3D). A further ex-vivo transdermal test showed that r-hirudin-loaded 3DMN can achieve transdermal r-hirudin delivery on rat skin or porcine cadaver skin. The cumulative transdermal amount of rat abdominal skin and porcine cadaver ear skin at 9 h was 31.37 ± 6.66 μg/cm^2 ($n = 4$) and 14.85 ± 0.24 μg/cm^2 ($n = 4$), respectively, suggested that the transdermal efficacy of 3DMN on rat skin was significantly higher than that on porcine cadaver skin (Fig. 4D & 4E). Diffusion coefficient (D_c) of both rat and porcine cadaver skin was further analyzed based on the Second Law of Fick, it showed that the D_c of rat skin was 2.03×10^{-6} (cm^2/h), significantly lower than the Dc of porcine cadaver skin: 2.87×10^{-5} (cm^2/h), but the flux of rat skin (1.26 μg/cm^{2}h) was significantly higher than porcine cadaver skin (0.17 μg/cm^{2}h). To exclude the activity loss of r-hirudin during the transdermal process at 37 °C, the anticoagulant activity of r-hirudin at many sampling time points was measured and the results showed that there was almost no activity loss detected during the process (Fig. S2E). In addition, the skin dissolution rate of 3DMN *in vivo* showed that $77.07\% \pm 2.39\%$ needle body can be quickly dissolved within 5 min, and the dissolution rate would slightly increase along with the extension of administration time such as $77.67\% \pm 2.25\%$ at 0.5 h and $84.39\% \pm 0.34\%$ at 1 h (Fig. 4A). Dosing rate was also detected to quantify the actual administration amount of r-hirudin via 3DMN, it is shown that the dosing rate of 3DMN on rat skin and porcine cadaver skin was, respectively $74.18\% \pm 5.51\%$ and $71.25\% \pm 8.29\%$ (Fig. 4B).

3.5. *Transdermal r-hirudin delivery via 3DMN in vivo*

To investigate the feasibility of MN administration, we further explored the transdermal r-hirudin delivery efficacy of 3DMN *in vivo*. Our results indicated that activated partial thromboplastin time (aPTT) (Fig. 5A), prothrombin time (PT) (Fig. 5B), and thrombin time (TT) (Fig. 5C) were significantly prolonged after r-hirudin treatment via SC and MN compared with the control group. aPTT, PT, and TT at 1 h post-administration in each group were further analyzed. The results showed that there was a significant time delay in r-hirudin SC-treated (0.5 mg/kg) and r-hirudin MN-treated rats. These data indicated that the 3DMN achieved transdermal r-hirudin delivery and subsequently exhibited an anticoagulant effect *in vivo*.

3.6. *Bioavailability of 3DMN patch*

To examine the *in vivo* efficacy of r-hirudin-loaded MNPs compared with IV and SC injection, changes in the serum r-hirudin concentrations were measured via LC-MS, and the pharmacokinetic parameters were summarized. T_{max} in the IV group was 1 min (Fig. 5D), whereas 30 min and

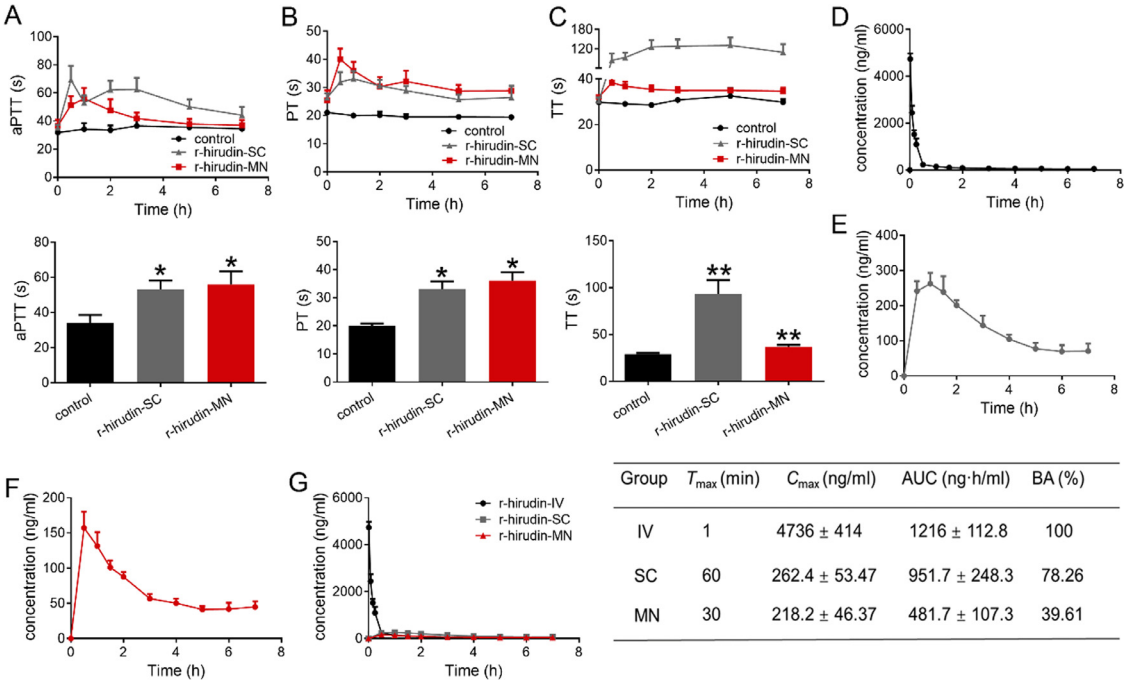

Group	T_{max} (min)	C_{max} (ng/ml)	AUC (ng·h/ml)	BA (%)
IV	1	4736 ± 414	1216 ± 112.8	100
SC	60	262.4 ± 53.47	951.7 ± 248.3	78.26
MN	30	218.2 ± 46.37	481.7 ± 107.3	39.61

Fig. 5 – Pharmacodynamics study of r-hirudin loaded in 3DMN patch (A-C). (A) aPTT at different time points in each group (above) and aPTT at 1 h (below), indicating the activation or inhibition of endogenous coagulation pathway and often used to monitor heparin dosage in clinical applications. (B) PT at different time points in each group (above) and PT at 1 h (below), demonstrating the exogenous coagulation system. (C) TT at different time points in each group (above) and TT at 1 h (below) reflects the time when fibrinogen is converted to fibrin which then directly reflects blood anticoagulant concentration. Pharmacokinetics study of r-hirudin *in vivo* (D-E). (D) The time-release curve of r-hirudin in IV group. (E) The time-release curve of r-hirudin in SC group. (F) The time-release curve of r-hirudin-loaded MN patch post-administration. (G) Pharmacokinetic parameters of r-hirudin post-application *in vivo*.

60 min were observed post-application for the MN and SC groups, respectively (Fig. 5E&5F). Thus, r-hirudin could achieve relatively slow drug release via MN administration. In parallel with delayed transdermal delivery of r-hirudin, the mean C_{max} was lower in the SC and MN groups compared to the IV group (IV: 4736 ± 414 ng/ml; SC: 262.4 ± 53.47 ng/ml; MN: 218.20±46.37 ng/ml). By comparing the AUCs to the IV group, the absolute bioavailability of the SC and MN groups was 78.26% and 39.61%, respectively (Fig. 5G). In summary, these data showed that r-hirudin combined with 3DMN could achieve a relatively friendly transdermal anticoagulant delivery.

3.7. *Skin toxicity and hemorrhage of r-hirudin delivery via 3DMN and SC*

For transdermal drug delivery, dermal toxicity could not be ignored, particularly for patients who received long-term administration. Skin toxicity of the drug and material can be reflected by observing the presence of redness, blotches, ulcers, and the severity on the skin after administration [48,49]. As shown in Fig. S4, no obvious redness, blotches, and ulcers were observed on the skin post administration and hair regrowth was observed four days later, and there were no obvious wounds remaining on the skin after hair removal. These preliminary results demonstrated that MN administration was minimally invasive and exhibited no skin toxicity.

A previous study revealed that SC injection of anticoagulants is always accompanied by postoperative bleeding [50,51]. Thus, we further observed hemorrhage in SD rats and C57BL/6 abdomen skin post-administrated via MNP and SC injection. There were obvious subcutaneous bruises that appeared in the SC group, while no bruises were observed in the MN administration group (Fig. 6A&6B). In addition, severe intracutaneous ecchymosis was also observed in the SC group after continuous administration of r-hirudin every half hour for three times, while almost no ecchymosis appeared in the MNP group (Fig. 6C). This indicated that administration of r-hirudin via MNP was superior to SC injection.

3.8. *Efficacy of 3DMN on acute pulmonary embolism model of mice*

We examined the protective effect of 3DMN in a model of lethal pulmonary thromboembolism induced by infusion with a 175 μl mixture of collagen (3.6 mg/ml) and epinephrine (0.03 mg/ml). Among control mice pretreated with saline, all mice died of widespread pulmonary thrombi and cardiac arrest within 5 min. In contrast, more than 53% of mice pretreated with r-hirudin via SC injection survived, and more

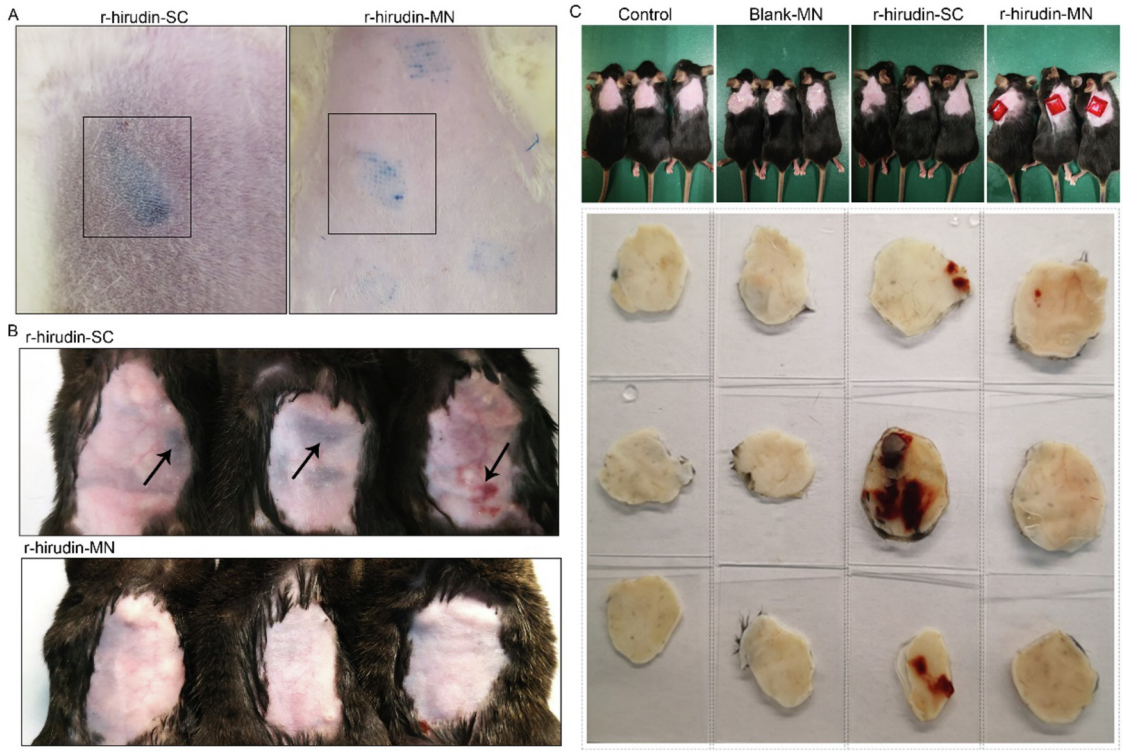

Fig. 6 – Hemorrhage of r-hirudin delivery via 3DMN and SC. (A) Administration of r-hirudin via MNP and SC injection on the abdomen skin of SD rats. (B) Administration of r-hirudin via MNP and subcutaneous injection on C57BL/6 abdomen skin daily for three days (methylene blue was added to the fabrication process of r-hirudin loaded MNs for better observation). (C) Representative images of intracutaneous ecchymosis after continuous administration of r-hirudin via MNP and SC every half hour for three times.

than 46% of mice pretreated with r-hirudin via MN survived (Fig. 7A&7B). Histological examination was performed to show different situations in which the vessels were obstructed by a thrombus. The results demonstrated that the vast majority of large and small vessels were obstructed by platelet- and thrombin-rich thrombi in the lungs of control mice, while there were few thrombi detectable in the lungs of r-hirudin-pretreated mice (Fig. 7C). Computed tomography revealed brighter areas in the saline group, however, these areas were not present in the r-hirudin injection and MN-treated groups (Fig. 7D). These results showed that r-hirudin-loaded MNs can prevent the subsequent formation of a pulmonary embolism.

3.9. *Efficacy of 3DMN on mesenteric artery thrombosis model of mice*

To examine the *in vivo* antithrombotic activity of r-hirudin-loaded MNs, we induced thrombosis in the mesenteric arterioles of mice by topical application of 10% $FeCl_3$, which triggers the formation of free radicals, thus injuring the vascular endothelium using intravital microscopy. As shown in Fig. 8A, thrombi formed more rapidly and stably in the mesenteric arterioles of saline-treated mice than in r-hirudin-loaded MN-treated mice. In untreated mice, multiple thrombi of $> 20\,\mu m$ were observed in the mesenteric arteriole 2 min after $FeCl_3$ injury. At 10 min, the vessel lumen was completely blocked by a stable, bulky thrombus. In contrast, mice pretreated with r-hirudin (0.5 mg/kg) via SC injection and MN administration before $FeCl_3$ injury exhibited decreased thrombus formation in the mesenteric arterioles compared to the mice receiving the same volume of saline. The emboli formation ratio ($> 20\,\mu m$) in 10 min was also markedly inhibited by r-hirudin (Fig. 8B). We observed the fluorescence length formed by calcein labeled platelets in the $FeCl_3$-injured thrombus at 10 min under a fluorescent inverted microscope. In the saline group, a longer length of fluorescence (1.50 ± 0.32 mm, $n = 11$) was formed; after the administration of r-hirudin (0.5 mg/kg, SC), the fluorescence length (0.22 ± 0.31 mm, $n = 24$) reduced significantly. Similar to the r-hirudin SC injection group, the fluorescence length in the MN group (0.14 ± 0.27 mm, $n = 24$) was also significantly reduced. Altogether, these data further confirmed the *in vivo* antithrombotic properties of r-hirudin when delivered via SC injection and MN administration.

3.10. *Fabrication and characterization of double-layer r-hirudin loaded MNs*

To minimize the dosage of r-hirudin during the MN fabrication process, double-layer MNs were explored to lock r-hirudin in the needles of the MNs array. Carmine, a water-soluble and alcohol-insoluble dye, was added to the fabrication process to serve as an indicator of r-hirudin (Fig. S5). Imaging records showed that distinct layering was observed at the interface

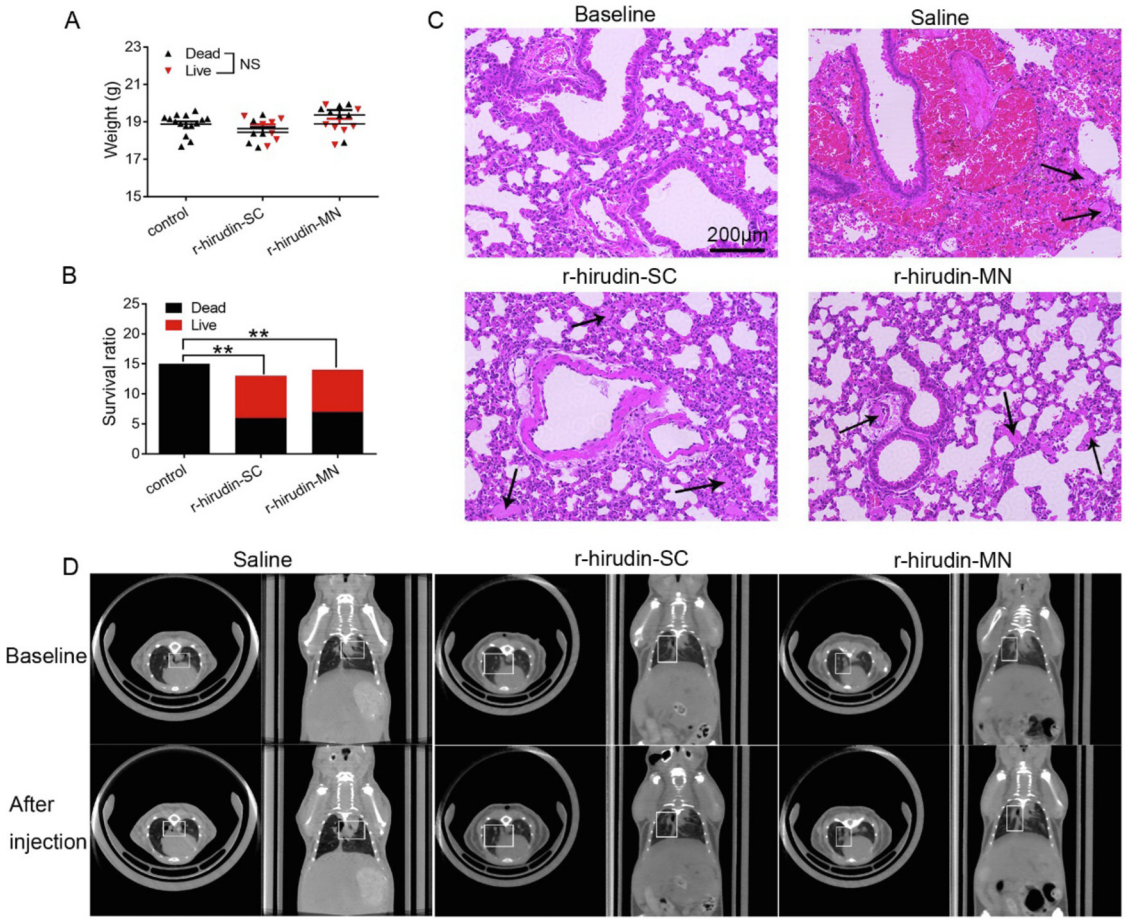

Fig. 7 – Efficacy of drug-loaded 3DMN patch on acute pulmonary embolism model of mice. (A) Bodyweight of C57 BL/6 mice in each group. (B) The survival rate of acute pulmonary embolism model in each group. (C) H&E staining of lung histologic section. (D) Representative images of lung tissue CT scan in each group.

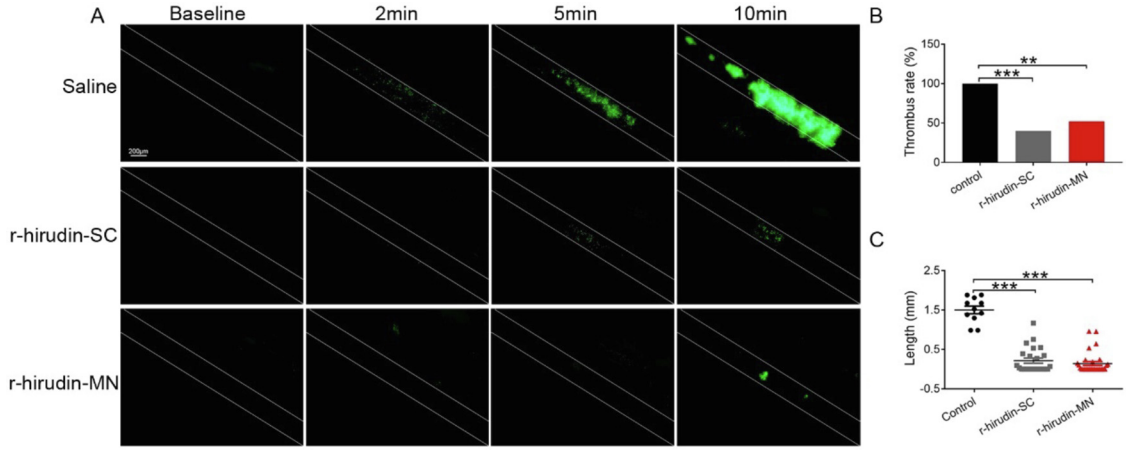

Fig. 8 – Efficacy of drug-loaded 3DMN patch on mesenteric artery thrombosis model of mice. (A) Representative image of mesenteric artery thrombosis within 10 min. (B) Emboli formation ratio at 10 min. (C) Fluorescence length of the $FeCl_3$-injured thrombus at 10 min.

of PVP and HA (Fig. S6). Strength tests of MNs loaded with different concentrations of r-hirudin were then conducted, and the fracture force of a single MN was significantly higher than 0.058 N (Fig. S7), which indicated that the drug-loaded double-layer MNs had the potential to penetrate the skin of the organism. The anticoagulant activity of double-layer drug-loaded MNs at a concentration of 10 mg/ml r-hirudin was close to the anticoagulant activity of single layer drug-loaded MNs at a concentration of 2.5 mg/ml r-hirudin (Fig. S8). These data showed that double-layer drug-loaded MNs could replace single-layer drug-loaded MNs to minimize drug usage.

3.11. *Discussion*

Since their proposal decades ago, MNs have attracted increasing interest because of their promising applications, particularly for clinical use [52,53]. The development of MNs necessitates the emergence of micro mould technology and MN fabrication materials. Thus, numerous biocompatible materials have emerged over the past few years. Nevertheless, in the micro-modeling field, photo etching has been the dominant even the complex manufacturing process and high technical requirements, owing to the absence of better alternatives, although many improved versions have emerged [54]. With the advent and maturity of 3D-printing technology, 3D-printed MNs array-mediated drug delivery has begun to be focused, and it can be easily fabricated via a single 3D printer within a few hours, indicating that it is more efficient than photoetching. Some 3D-printed products have also been successfully applied in clinical, like microsensors for detecting the microcirculation of organisms, drug-coated MNs for transdermal drug delivery, and micro-receivers for specimen collection [55,56].

As for the application of 3D printing in the MN field, biodegradable 3D printing MN arrays have been reported via direct loading of the target drug into the printing material [45]. This would be a significant breakthrough in drug-loaded MNs fabrication. However, the pretreatment process before printing would be selective to the delivered drugs, and this type of printing material would not be economical and diversiform. Therefore, we assumed that if we could duplicate the 3D printing MNs array with PDMS to obtain a model that could be directly used for MNs fabrication, then MNs can be fabricated based on current existing biodegradable materials and methods. Our previous study showed that PDMS cannot be solidified at the interface of the photosensitive resin. Thus, we attempted to find a mediated material to replace PDMS in the first step, and gelatine was selected based on its features such as softness and solidification at room temperature so that the 3D-printing micro mold was not damaged during the duplicate process. Finally, we obtained the PDMS mould that could be directly used for MNs fabrication via a three-step casting process (Fig. 3A&3B). To our knowledge, this is the first study to create a method for the translation of a 3D-printing MNs array into a PDMS mould and successfully apply it to MNs fabrication.

We also noticed the resolution differences between the photo etching and 3D-printing techniques. There is a slight pinpoint loss of the 3D printing MNs array model, and the three-step casting process would further reduce the resolution of the MN tip, however, it doesn't have an obvious influence on the height of microneedles. On the contrary, the height of HA-based 3DMN was sometimes a little higher than the printed MNs array model when demould completely, it is thought to be caused by the feature of gelatine which would experience slight retraction after the loss of water during PDMS solidification. In addition, there was also a minor difference in the height and shape of HA-based 3DMN observed, it might be resulted from demolding or ambient humidity fluctuation when imaging. In addition, the penetration depth was also detected and found significantly shorter than MNs height, we think it would be a consequence of MNs dissolving or breaking during insertion or the penetration depth was decided by the thickness of skin. Although a few minor flaws existed, it does not affect the transdermal delivery ability of r-hirudin, in contrast, the design and acquisition of MNs would be more diverse and rapid via 3D printing.

R-hirudin is a direct thrombin inhibitor produced by our lab. Based on our previous study, r-hirudin exhibited high affinity and specificity for thrombin. However, in clinical trials, r-hirudin was administered via IV or SC injection, which is usually accompanied by postoperative bleeding, poor patient compliance and inconvenience of daily medication, thus limiting its clinical application. Therefore, we hypothesized that if r-hirudin could achieve transdermal delivery via 3DMN, and then the feasibility and practicability of 3DMN can also be further verified. Our results showed that r-hirudin-loaded 3DMN can withstand a certain force, penetrate porcine or rat skin, and then release r-hirudin, which is more in keeping with clinical medication needs. Further study showed that the *in vivo* absolute and relative bioavailability of r-hirudin loaded 3DMN was around ~ 40% and ~ 50%, significantly lower than the already reported drug-loading MNs. We then explored the causes leading to low bioavailability and found that the main reason would be the dosing rate which cannot reach 100% after administration, it was around ~70% *in vitro* according to our study and would be lower *in vivo*. Further investigation showed that r-hirudin can be transported to blood rapidly within hours via the 3DMN and effectively alleviate embolism formation *in vivo*. Furthermore, no bleeding was observed post-administration, which greatly facilitated the daily use of medicine and improved medication safety. These results indicate that our 3DMN is feasible for transdermal r-hirudin delivery. In addition, our 3DMN may also provide strategies for transdermal delivery of other anticoagulants, and personalized customization of MNs would be realized via 3D printing.

4. Conclusion

In conclusion, we explored a route for MN mould fabrication originating from a 3D printed MNs array model via a three-step casting process, which would supplement the inadequacy of existing micro-mold manufacturing processes, such as high cost and complexity. Application of the 3DMN for the transdermal delivery of r-hirudin cannot only prevents thrombosis in vascular embolic disease, but also prevents many side effects that are common in clinical use via SC or IV

injection, which greatly facilitates the daily use of medicine. In addition to diversifying the type of MNs and achieving personalized customization, a systematic strategy for MNs acquisition based on the 3D printing technique ranging from MNs model design to drug-loaded MNs application would provide ideas for the transdermal administration of many other drugs, especially anticoagulants.

Conflicts of interest

The authors report no conflicts of interest. The authors alone are responsible for the content and writing of this article.

Acknowledgement

This study was supported by the National Natural Science Foundation of China (NSFC 81902995) and the project funded by China Postdoctoral Science Foundation (2018M641936).

The authors would like to thank professor Mo Wei for his premortal contribution to the guidance of this work. Thanks for his support and participation in project design and implementation.

REFERENCES

[1] Myers K, Lyden A. A review on the new and old anticoagulants. Orthop Nurs 2019;38(1):43–52.
[2] Piran S, Schulman S. Treatment of bleeding complications in patients on anticoagulant therapy. Blood 2019;133(5):425–35.
[3] Burr N, Lummis K, Sood R, Kane JS, Corp A, Subramanian V. Risk of gastrointestinal bleeding with direct oral anticoagulants: a systematic review and network meta-analysis. Lancet Gastroenterol Hepatol 2017;2(2):85–93.
[4] Anselmo AC, Gokarn Y, Mitragotri S. Non-invasive delivery strategies for biologics. Nat Rev Drug Discov 2019;18(1):19–40.
[5] Indermun S, Luttge R, Choonara YE, Kumar P, du Toit LC, Modi G, et al. Current advances in the fabrication of microneedles for transdermal delivery. J Control Release 2014;185:130–8.
[6] Huang Y, Zhang Y, Zhao B, Xu Q, Zhou X, Song H, et al. Structural basis of RGD-hirudin binding to thrombin: tyr3 and five C-terminal residues are crucial for inhibiting thrombin activity. BMC Struct Biol 2014;14:26.
[7] Li YR, Huang YN, Zhao B, Wu MF, Li TY, Zhang YL, et al. RGD-hirudin-based low molecular weight peptide prevents blood coagulation via subcutaneous injection. Acta Pharmacol Sin 2020;41(6):753–62.
[8] Wang M, Hu L, Xu C. Recent advances in the design of polymeric microneedles for transdermal drug delivery and biosensing. Lab Chip 2017;17(8):1373–87.
[9] Sullivan SP, Murthy N, Prausnitz MR. Minimally invasive protein delivery with rapidly dissolving polymer microneedles. Adv Mater 2008;20(5):933–8.
[10] Park JH, Allen MG, Prausnitz MR. Polymer microneedles for controlled-release drug delivery. Pharm Res 2006;23(5):1008–19.
[11] Qiu Y, Li C, Zhang S, Yang G, He M, Gao Y. Systemic delivery of artemether by dissolving microneedles. Int J Pharm 2016;508(1–2):1–9.
[12] Gualeni B, Coulman SA, Shah D, Eng PF, Ashraf H, Vescovo P, et al. Minimally invasive and targeted therapeutic cell delivery to the skin using microneedle devices. Br J Dermatol 2018;178(3):731–9.
[13] Duong HTT, Yin Y, Thambi T, Kim BS, Jeong JH, Lee DS. Highly potent intradermal vaccination by an array of dissolving microneedle polypeptide cocktails for cancer immunotherapy. J Mater Chem B 2020;8(6):1171–81.
[14] Permana AD, Paredes AJ, Volpe-Zanutto F, Anjani QK, Utomo E, Donnelly RF. Dissolving microneedle-mediated dermal delivery of itraconazole nanocrystals for improved treatment of cutaneous candidiasis. Eur J Pharma Biopharma 2020;154:50–61.
[15] Rojekar S, Vora LK, Tekko IA, Volpe-Zanutto F, McCarthy HO, Vavia PR, et al. Etravirine-loaded dissolving microneedle arrays for long-acting delivery. Eur J Pharma Biopharma 2021;165:41–51.
[16] Yan QY, Wang WW, Weng JQ, Zhang ZH, Yin LN, Yang QL, et al. Dissolving microneedles for transdermal delivery of huperzine A for the treatment of Alzheimer's disease. Drug Deliv 2020;27(1):1147–55.
[17] Yang H, Kang G, Jang M, Um DJ, Shin J, Kim H, et al. Development of lidocaine-loaded dissolving microneedle for rapid and efficient local anesthesia. Pharmaceutics 2020;12(11).
[18] Arya JM, Dewitt K, Scott-Garrard M, Chiang YW, Prausnitz MR. Rabies vaccination in dogs using a dissolving microneedle patch. J Control Release 2016;239:19–26.
[19] Edens C, Collins ML, Ayers J, Rota PA, Prausnitz MR. Measles vaccination using a microneedle patch. Vaccine 2013;31(34):3403–9.
[20] Choi IJ, Kang A, Ahn MH, Jun H, Baek SK, Park JH, et al. Insertion-responsive microneedles for rapid intradermal delivery of canine influenza vaccine. J Control Release 2018;286:460–6.
[21] Hutton ARJ, Quinn HL, McCague PJ, Jarrahian C, Rein-Weston A, Coffey PS, et al. Transdermal delivery of vitamin K using dissolving microneedles for the prevention of vitamin K deficiency bleeding. Int J Pharm 2018;541(1–2):56–63.
[22] Ling MH, Chen MC. Dissolving polymer microneedle patches for rapid and efficient transdermal delivery of insulin to diabetic rats. Acta Biomater 2013;9(11):8952–61.
[23] Lee JW, Choi SO, Felner EI, Prausnitz MR. Dissolving microneedle patch for transdermal delivery of human growth hormone. Small 2011;7(4):531–9.
[24] Zhang YQ, Yu JC, Wang JQ, Hanne NJ, Cui Z, Qian CG, et al. Thrombin-responsive transcutaneous patch for auto-anticoagulant regulation. Adv. Mater. 2017;29(4).
[25] Monkare J, Nejadnik MR, Baccouche K, Romeijn S, Jiskoot W, Bouwstra JA. IgG-loaded hyaluronan-based dissolving microneedles for intradermal protein delivery. J. Controlled Release 2015;218:53–62.
[26] Waghule T, Singhvi G, Dubey SK, Pandey MM, Gupta G, Singh M, et al. Microneedles: a smart approach and increasing potential for transdermal drug delivery system. Biomed Pharmacother 2019;109:1249–58.
[27] Prausnitz MR. Engineering microneedle patches for vaccination and drug delivery to skin. Annu Rev Chem Biomol Eng 2017;8(8):177–200.
[28] Makvandi P, Kirkby M, Hutton ARJ, Shabani M, Yiu CKY, Baghbantaraghdari Z, et al. Engineering Microneedle Patches for Improved Penetration: analysis, skin models and factors affecting needle insertion. Nanomicro Lett 2021;13(1):93.
[29] Lee IC, Lin WM, Shu JC, Tsai SW, Chen CH, Tsai MT. Formulation of two-layer dissolving polymeric microneedle patches for insulin transdermal delivery in diabetic mice. J Biomed Mater Res Part A 2017;105(1):84–93.
[30] Wu Y, Vora LK, Wang Y, Adrianto MF, Tekko IA, Waite D, et al. Long-acting nanoparticle-loaded bilayer microneedles

for protein delivery to the posterior segment of the eye. Eur J Pharm Biopharm 2021;165:306–18.
[31] Caudill CL, Perry JL, Tian S, Luft JC, DeSimone JM. Spatially controlled coating of continuous liquid interface production microneedles for transdermal protein delivery. J Controll Release 2018;284:122–32.
[32] Palo M, Hollander J, Suominen J, Yliruusi J, Sandler N. 3D printed drug delivery devices: perspectives and technical challenges. Expert Rev Med Dev 2017;14(9):685–96.
[33] Economidou SN, Douroumis D. 3D printing as a transformative tool for microneedle systems: recent advances, manufacturing considerations and market potential. Adv Drug Deliv Rev 2021;173:60–9.
[34] Lim SH, Kathuria H, Amir MHB, Zhang X, Duong HTT, Ho PC, et al. High resolution photopolymer for 3D printing of personalised microneedle for transdermal delivery of anti-wrinkle small peptide. J Control Release 2021;329:907–18.
[35] Rahbari R, Ichim I, Bamsey R, Burridge J, Guy OJ, Bolodeoku J, et al. Characterisation of drug delivery efficacy using microstructure-assisted application of a range of APIs. Pharmaceutics 2020;12(12).
[36] Szeto B, Aksit A, Valentini C, Yu M, Werth EG, Goeta S, et al. Novel 3D-printed hollow microneedles facilitate safe, reliable, and informative sampling of perilymph from guinea pigs. Hear Res 2021;400:108141.
[37] Wu MX, Zhang YJ, Huang H, Li JW, Liu HY, Guo ZY, et al. Assisted 3D printing of microneedle patches for minimally invasive glucose control in diabetes. Mater Sci Eng C Mater Biol Appl 2020:117.
[38] Uddin MJ, Scoutaris N, Economidou SN, Giraud C, Chowdhry BZ, Donnelly RF, et al. 3D printed microneedles for anticancer therapy of skin tumours. Mater Sci Eng C Mater Biol Appl 2020;107:110248.
[39] Chen Y, Chen BZ, Wang QL, Jin X, Guo XD. Fabrication of coated polymer microneedles for transdermal drug delivery. J Control Release 2017;265:14–21.
[40] Larraneta E, Henry M, Irwin NJ, Trotter J, Perminova AA, Donnelly RF. Synthesis and characterization of hyaluronic acid hydrogels crosslinked using a solvent-free process for potential biomedical applications. Carbohydr Polym 2018;181:1194–205.
[41] Kathuria H, Kang K, Cai J, Kang L. Rapid microneedle fabrication by heating and photolithography. Int J Pharm 2020;575:118992.
[42] Aung NN, Ngawhirunpat T, Rojanarata T, Patrojanasophon P, Opanasopit P, Pamornpathomkul B. HPMC/PVP dissolving microneedles: a promising delivery platform to promote trans-epidermal delivery of alpha-arbutin for skin lightening. AAPS PharmSciTech 2019;21(1).
[43] Su S, Yu Y, Mo W, Zhang Y, Song H, Chen Q, et al. A development of LC-MS method combining ultrafiltration and lyophilization for determination of r-RGD-Hirudin in human serum. J Chromatogr B Analyt Technol Biomed Life Sci 2008;870(1):27–31.
[44] Hu L, Fan Z, Du H, Ni R, Zhang S, Yin K, et al. BF061, a novel antiplatelet and antithrombotic agent targeting P2Y(1)(2) receptor and phosphodiesterase. Thromb Haemost, 2011;106(6):1203–14.
[45] Luzuriaga MA, Berry DR, Reagan JC, Smaldone RA, Gassensmith JJ. Biodegradable 3D printed polymer microneedles for transdermal drug delivery. Lab Chip 2018;18(8):1223–30.
[46] Hsu WL, Huang CY, Hsu YP, Hwang TL, Chang SH, Wang HYJ, et al. On-skin glucose-biosensing and on-demand insulin-zinc hexamers delivery using microneedles for syringe-free diabetes management. Chem Eng J 2020:398.
[47] Trombino S, Servidio C, Curcio F, Cassano R. Strategies for hyaluronic acid-based hydrogel design in drug delivery. Pharmaceutics 2019;11(8).
[48] Chandra SA, Stokes AH, Hailey R, Merrill CL, Melich DH, DeSmet K, et al. Dermal toxicity studies: factors impacting study interpretation and outcome. Toxicol Pathol 2015;43(4):474–81.
[49] Kandarova H, Bendova H, Letasiova S, Coleman KP, De Jong WH, Jirova D. Evaluation of the medical devices benchmark materials in the controlled human patch testing and in the RhE *in vitro* skin irritation protocol. Toxicol *In Vitro* 2018;50:433–8.
[50] Jareño-Collado R, Sánchez-Sánchez MM, Fraile-Gamo MP, García-Crespo N, Barba-Aragón S, Bermejo-García H, et al. Ecchymosis and/or haematoma formation after prophylactic administration of subcutaneous enoxaparin in the abdomen or arm of the critically ill patient. Enfermería Intensiva (English ed.) 2018;29(1):4–13.
[51] Mohammady M, Janani L, Sari AA. Slow *versus* fast subcutaneous heparin injections for prevention of bruising and site pain intensity. Cochrane Database Syst Rev 2017;10:CD008077.
[52] Larraneta E, Lutton REM, Woolfson AD, Donnelly RF. Microneedle arrays as transdermal and intradermal drug delivery systems: materials science, manufacture and commercial development. Mater Sci Eng R Rep 2016;104:1–32.
[53] Bae WG, Ko H, So JY, Yi H, Lee CH, Lee DH, et al. Snake fang-inspired stamping patch for transdermal delivery of liquid formulations. Sci Transl Med 2019;11(503).
[54] Singh P, Carrier A, Chen Y, Lin S, Wang J, Cui S, et al. Polymeric microneedles for controlled transdermal drug delivery. J Control Release 2019;315:97–113.
[55] Al Sulaiman D, Chang JYH, Bennett NR, Topouzi H, Higgins CA, Irvine DJ, et al. Hydrogel-coated microneedle arrays for minimally invasive sampling and sensing of specific circulating nucleic acids from skin interstitial fluid. ACS Nano 2019;13(8):9620–8.
[56] Yin M, Xiao L, Liu Q, Kwon SY, Zhang Y, Sharma PR, et al. 3D printed microheater sensor-integrated, drug-encapsulated microneedle patch system for pain management. Adv Healthc Mater 2019:e1901170.